

1	Supporting Methods	63
2	The systems were solvated using the SOLVATE plugin in VMD(2) and neutralizing ions were added to bring the system to a	64
3	0.15M salt concentration using the AUTOIONIZE plugin. The final system contained about 160,000 atoms. MUTATE plugin	65
4	was used to introduce the K289M mutation in the γ subunit of GABA _A R receptor.	66
5	All bonds to the hydrogen atoms were constrained using the SHAKE/RATTLE algorithm. A multiple time-step rRESPA	67
6	method was used, and controlled with a high frequency time-step of 2fs and low frequency time-step of 4fs. All the systems	68
7	were energy minimized for 10000 steps, then simulated for 5 ns with restraints of 1 kcal/mol/Å applied to the C _α atoms of the	69
8	protein. Restraints were then removed and 495 ns of nearly unrestrained simulation was carried out in all four systems at	70
9	low temperature. During this period of the simulation, only harmonic restraints (force constant 0.4 kcal/mol/Å) between the	71
10	intracellular ends of the M3 and M4 helices were used, to mimic the effects of the intracellular domain and prevent separation	72
11	of the M4 helix from the rest of the bundle.	73
12		74
13	Long-range electrostatics. The simulations here used the prescribed cutoff value of 12 Å for the CHARMM forcefield, with a	75
14	switching function past 10Å, combined with PME and a grid size of about 1Å. The distances between charged residues in	76
15	the interfacial band are similar to this cutoff distance, and it is not uncommon to use cutoffs less than 10Å(as in (?)). This	77
16	may cause a significant accumulated error in simulations of any proteins with repeated interactions near the cutoff/switching	78
17	distance, not just pLGICs. In pLGICs, it can reduce the energetic cost of shrinking the interfacial band, leading to an increased	79
18	likelihood of closed states even in WT systems. By recalculating energies using direct Coulomb electrostatics just for interfacial	80
19	band and pore oscillator residues, from a trajectory generated using PME, we found PME reduced the energetic difference	81
20	between elongated and regular conformations by about 5 kcal/mol.	82
21		83
22	SMD Simulations. Steered Molecular Dynamics (SMD) simulations (3, 4) were used to obtain favorable positions of the ion at	84
23	different positions along the channel, for later use in Adaptive Biasing Force (ABF) calculations. The chloride ion was pulled	85
24	along the pore of the channel at a constant velocity of 10Å/ns. The force required to pull at constant velocity is also calculated,	86
25	and can, in principle, be used to calculate a potential of mean force (PMF) using Jarzynski's equation (5, 6), but in practice it	87
26	is challenging to achieve a sufficiently slow pulling speed.	88
27		89
28	ABF Simulations. Adaptive biasing force calculations (ABF)(? ? ? ?) were used to measure the potential of mean force	90
29	(PMF) of a chloride ion translocating the GABA _A R ion channel at 315K, for both the WT and K289M channels. ABF was	91
30	performed using the Collective Variables module(?) of NAMD2.9. The pore axis was divided into 23 bins of each 5Å length.	92
31	Initial coordinates for the ion were obtained from SMD simulations (as described in SI). One thousand samples were collected	93
32	in each bin prior to the application of ABF to avoid undesired non-equilibrium effects on the dynamics. Fifteen ns of trajectory	94
33	were generated in most bins, while bins near the primary barrier in the pore contained 25 ns.	95
34		96
35	Pore Analysis. Measurement and analysis of the pore radii has been carried out using the HOLE software (7) and TCL scripting	97
36	through VMD(2). Python scripts have been used to analyze and visualize the hydration of the pore throughout the simulation.	98
37		99
38	Poisson-Boltzmann Calculations. The Poisson-Boltzmann (PB) profile for conduction of both a Na ⁺ and Cl ⁻ through the ion	100
39	channel was calculated using APBSmem(8). The pre-generated PQR format of the proteins using PDB2PQR(9) tool was used	101
40	as the input for the electrostatic potential calculations.	102
41	These calculations were performed for initial non-equilibrated structures of the protein, as well as for conformations extracted	103
42	from the last 50 ns of both the 300K and 315K MD simulations (for Cl ⁻).	104
43		105
44	Graphs and images. All plots were calculated and drawn using Python and Tcl scripts. In Figure 2 and the similar supplementary	106
45	figures S5-S11, the series of curves depicting the pore-opening events were further smoothed using a digital filter(Butterworth)	107
46	with a order of the filter value, 2, and a critical frequency value, 0.02, as implemented in the SciPy python module. The time	108
47	derivative of the minimum pore radius was calculated using the gradient function implemented in the numpy python module.	109
48	VMD(2) was used for visualization and for creating molecular images and movies.	110
49		111
50	Supporting Theory	112
51	We consider an irregular pentagon with five side lengths r_i and five diagonal lengths s_i (Figure S1A). The total Coulomb	113
52	energy for the charged ring is given by	114
53		115
54	$U_{+5} = k_e e^2 \sum_i^5 \frac{1}{r_i} + \sum_i^5 \frac{1}{s_i}$	[1]
55		116
56		117
57	where e is the electron charge, $k_e = 332\text{Å}/\text{kcal/mol}/e^2$ is the Coulomb constant. Writing each distance as a perturbation from	118
58	the average : $r_i = \bar{r}(1 + \delta r_i)$ and $s_i = \bar{s}(1 + \delta s_i)$, where the average adjacent length $\bar{r} = \sum_i^5 r_i/5$ and the average diagonal	119
59		120
60		121
61		122
62		123
		124

125 length $\bar{s} = \sum_i^5 s_i/5$. Expanding in powers of δs_i and δr_i ,

$$\begin{aligned} \sum_j^5 \frac{1}{r_j} &= \sum_j^5 \frac{1}{\bar{r}(1 + \delta r_i)} = \frac{1}{\bar{r}} \sum_j^5 (1 - \delta r_i + O(\delta r_i^2)) \\ &= \frac{5}{\bar{r}} \left(1 + O(\bar{\delta r}^2) \right) \end{aligned}$$

132 and similarly,

$$\sum_j^5 \frac{1}{s_j} = \frac{5}{\bar{s}} \left(1 + O(\bar{\delta s}^2) \right),$$

137 where we have used $\sum_j^5 \delta s_j = \sum_j^5 \delta r_j = 0$, and $\bar{\delta r}^2$ and $\bar{\delta s}^2$ are the variance in r and s across the five sides of the pentagon
138 respectively. Therefore,

$$U_{+5} = k_e e^2 \left(\sum_i^5 \frac{1}{r_i} \right) \left(1 + \frac{\sum_j^5 \frac{1}{s_j}}{\sum_j^5 \frac{1}{r_j}} \right)$$

$$= k_e e^2 \left(\frac{5}{\bar{r}} \left(1 + O(\bar{\delta r}^2) \right) \right) \left(1 + \frac{\frac{5}{\bar{s}}(1 + O(\bar{\delta s}^2))}{\frac{5}{\bar{r}}(1 + O(\bar{\delta r}^2))} \right)$$

$$= \frac{5k_e e^2}{\bar{r}} \left(1 + \frac{\bar{r}}{\bar{s}} \right) + O(\bar{\delta r}^2) + O(\bar{\delta s}^2)$$

148 For a symmetric pentagon $\bar{s} = \phi \bar{r}$ where $\phi \equiv (1 + \sqrt{5})/2 \sim 1.62$ is a geometric constant usually called the “golden ratio”,
149 representing the ratio between the lengths of a pentagon diagonal and side, and with the convenient property $1/\phi = \phi - 1 = 0.62$.
150 We define δ_ϕ as the deviation of $\frac{\bar{r}}{\bar{s}}$ from $1/\phi = \phi - 1 = 0.62$, so $\delta_\phi \equiv \frac{\bar{r}}{\bar{s}} - (\phi - 1)$, and

$$U_{+5} = \frac{5k_e e^2 \phi}{\bar{r}} \left(1 + \frac{\delta_\phi}{\phi} \right) + O(\bar{\delta r}^2) + O(\bar{\delta s}^2)$$

155 The linear term in δ_ϕ reflects the effects of asymmetry on the relative contributions of diagonal and adjacent distances.
156 Second-order terms given by $\bar{\delta r}^2$ and $\bar{\delta s}^2$ reflect variance in the adjacent and diagonal distances respectively. According to
157 Eq. 8, positive values of δ_ϕ (in which diagonal distances are shorter than expected in a regular pentagon) will increase the
158 overall energy of the interfacial band, provided the average distance between adjacent residues (\bar{r}) is kept constant. This
159 asymmetry-induced increase in energy can be offset by an overall increase in the size of the interfacial band : $\delta_\phi > 0$ will
160 stabilize a larger \bar{r} . Similarly, negative δ_ϕ will decrease the overall energy of the interfacial band and allow it to decrease the
161 average separation \bar{r} with reduced penalty.

162 Any reduction in δ_ϕ will thus destabilize the open state. We ran simple numerical calculations to determine how increased
163 random noise would affect the distribution of δ_ϕ . Five points were generated with random polar angles corresponding to
164 $\{0 + \zeta_1, 2\pi/5 + \zeta_2, 4\pi/5 + \zeta_3, 6\pi/5 + \zeta_4, 8\pi/5 + \zeta_5\}$ where ζ_i was a random value taken from a flat distribution in the range $\pm 3\pi/40$
165 (low variation) or in the range $\pm 5\pi/40$ (high variation), and the radial values were $\{1.5 + \rho_1, 1.5 + \rho_2, 1.5 + \rho_3, 1.5 + \rho_4, 1.5 + \rho_5\}$
166 where ρ_i was a random value from a flat distribution in the range ± 0.375 (low variation) or ± 0.625 (high variation). Although
167 these are the specific values used in Figure S2 and are given for completeness, the overall trends were not particularly sensitive
168 to the precise values chosen.

249
250
251
252
253
254
255
256
257
258
259
260
261
262
263
264
265
266
267
268
269
270
271
272
273
274
275
276
277
278
279
280
281
282
283
284
285
286
287
288
289
290
291
292
293
294
295
296
297
298
299
300
301
302
303
304
305
306
307
308
309
310

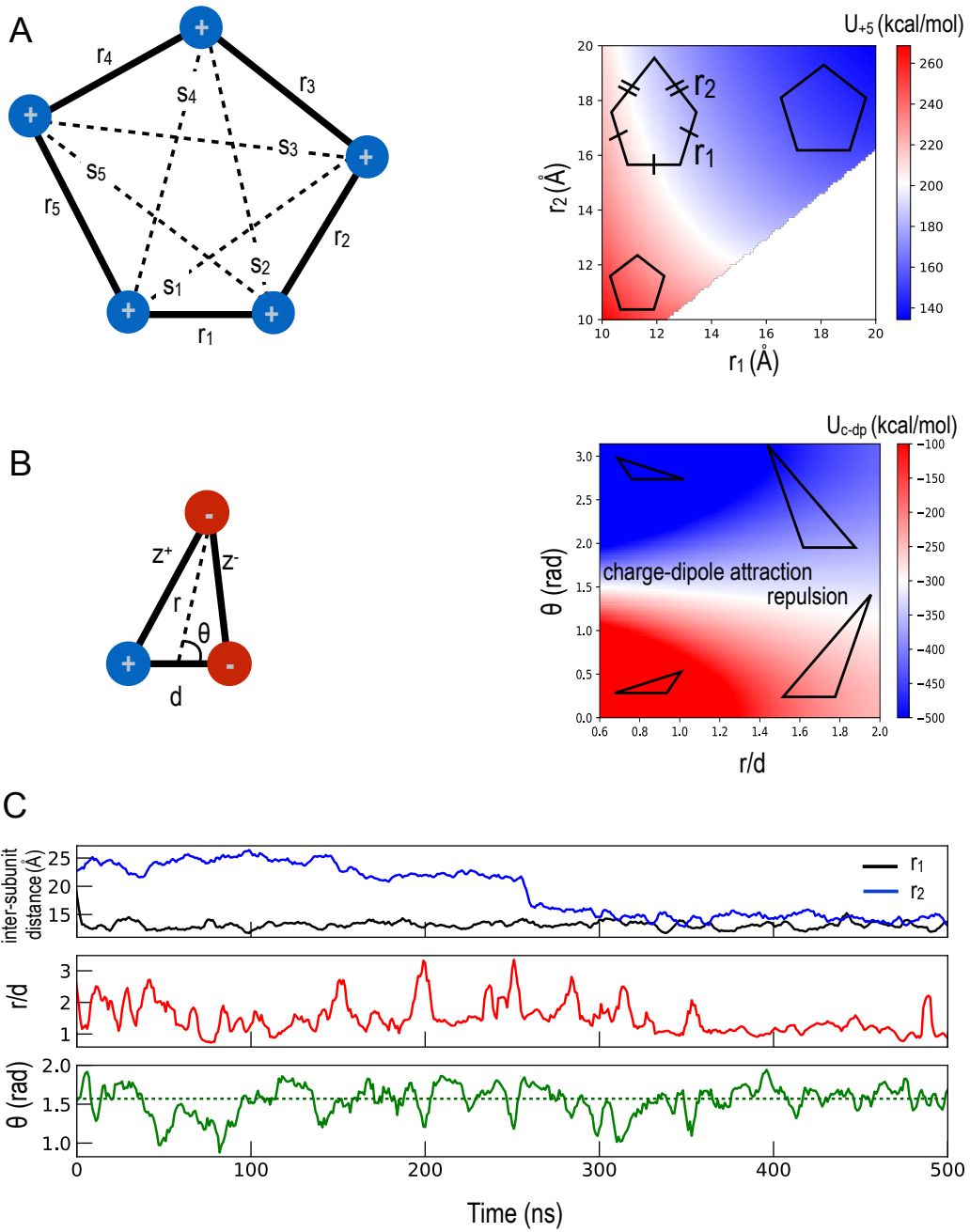
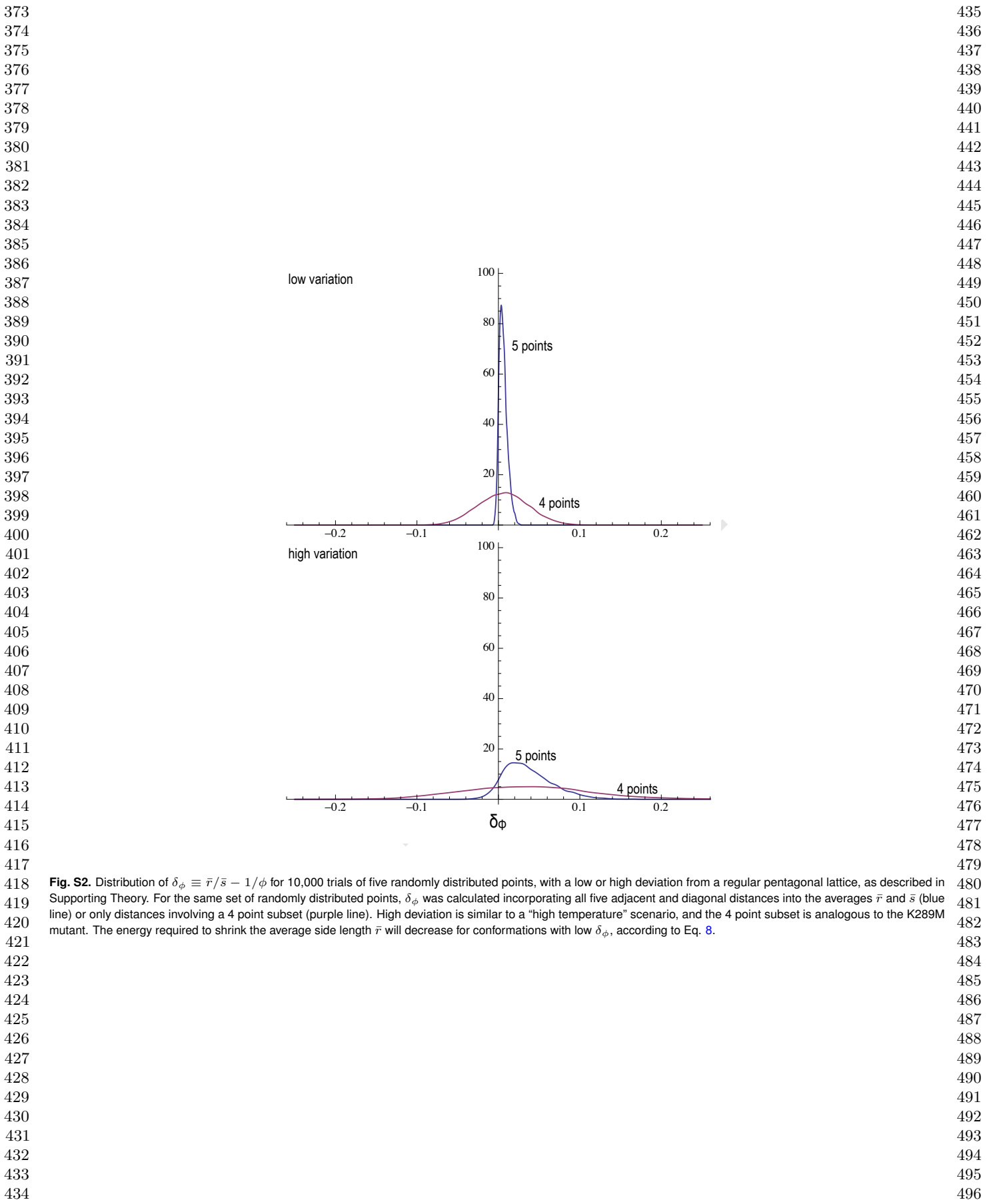


Fig. S1. (A) Adjacent and diagonal distances for the pentagonal Interfacial Band used to calculate averages for Eq. 8, and the associated electrostatic energy for the special case of a pentagon in which three sides are identical and two adjacent sides are also identical, but may differ from the other three. This special case is similar to that observed for the symmetrization step in Figure 2. (B) Definition of terms for the charge-dipole interaction that is formed by three residues in the pore oscillator, as well as associated energy. At around $\theta = \pi/2$, the potential energy shifts from decreasing with increasing distance (repulsive) to increasing with increasing distance (attractive). (C) Trajectory for defined angles and distances for the K315 replica explored in Figure 2; curves shown here are smoothed much less than in Figure 2 and retain significantly more high frequency noise.

311
312
313
314
315
316
317
318
319
320
321
322
323
324
325
326
327
328
329
330
331
332
333
334
335
336
337
338
339
340
341
342
343
344
345
346
347
348
349
350
351
352
353
354
355
356
357
358
359
360
361
362
363
364
365
366
367
368
369
370
371
372



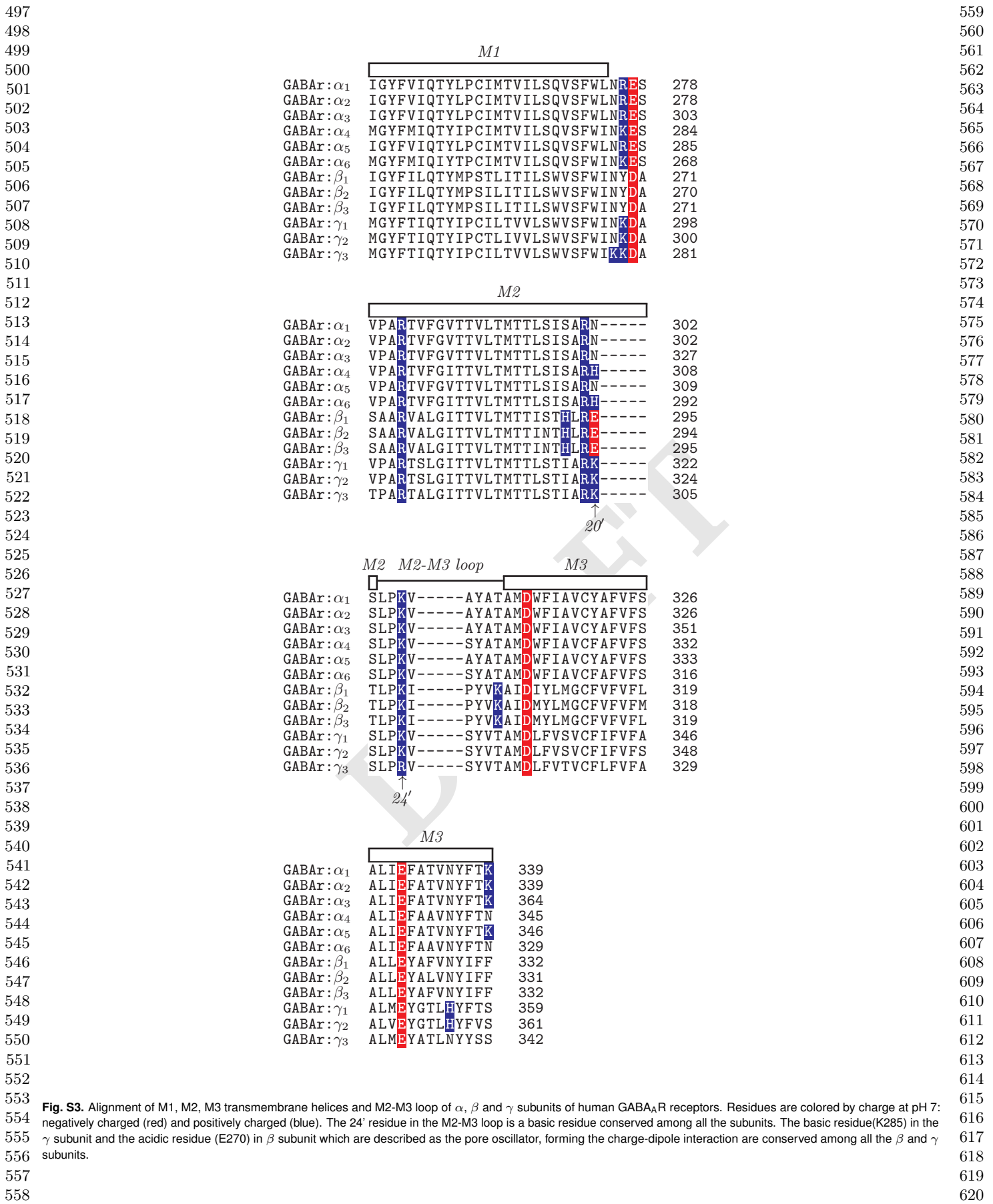
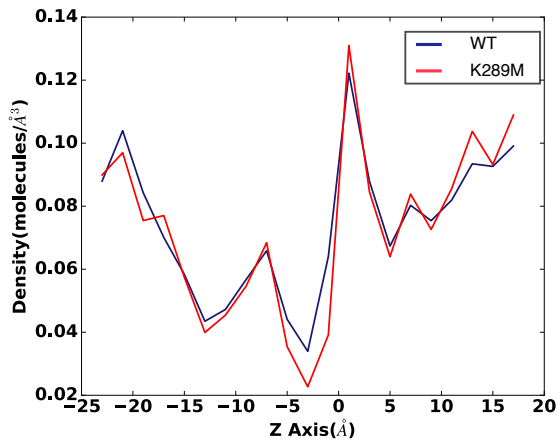


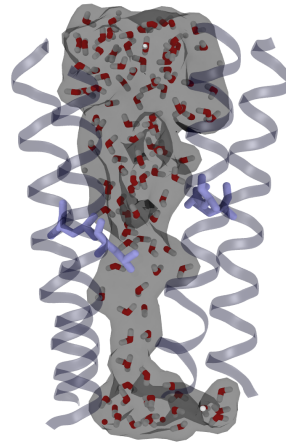
Fig. S3. Alignment of M1, M2, M3 transmembrane helices and M2-M3 loop of α , β and γ subunits of human GABA_AR receptors. Residues are colored by charge at pH 7: negatively charged (red) and positively charged (blue). The 24' residue in the M2-M3 loop is a basic residue conserved among all the subunits. The basic residue(K285) in the γ subunit and the acidic residue (E270) in β subunit which are described as the pore oscillator, forming the charge-dipole interaction are conserved among all the β and γ subunits.

621
622
623
624
625
626
627
628
629
630
631
632
633
634
635
636
637
638
639
640
641
642

A



B



C

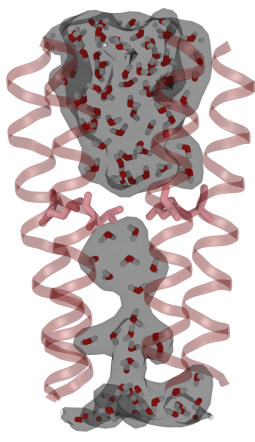
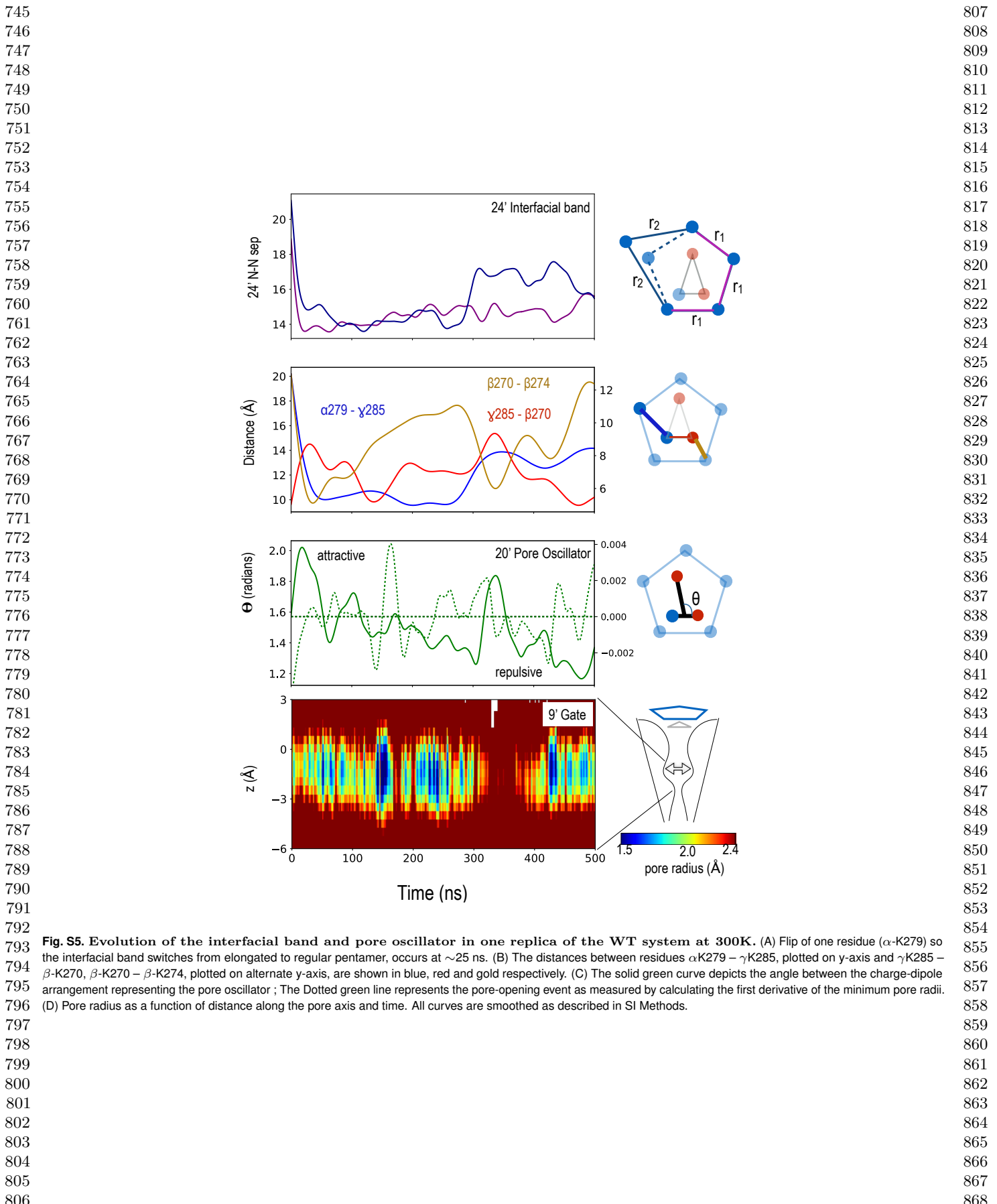
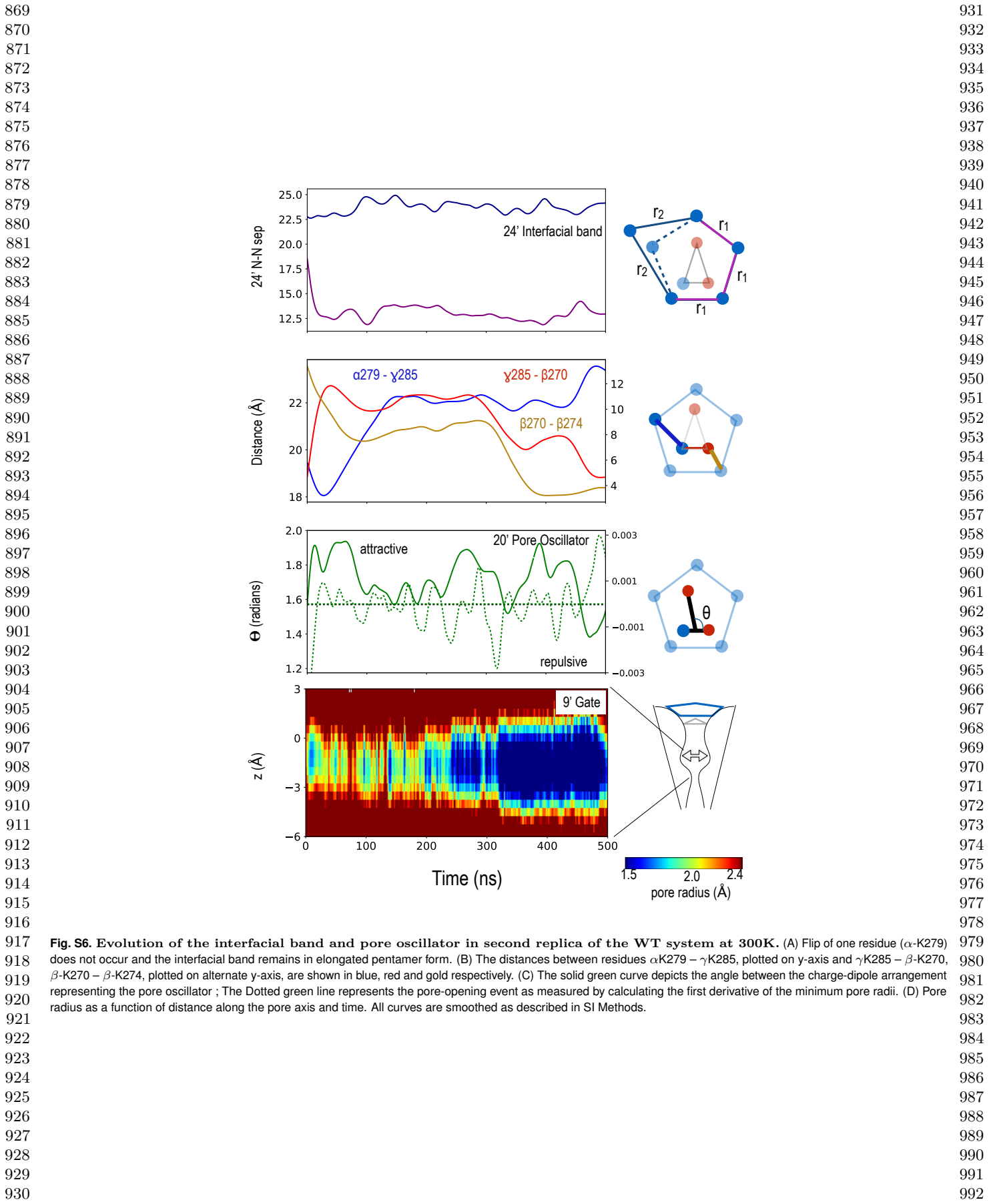
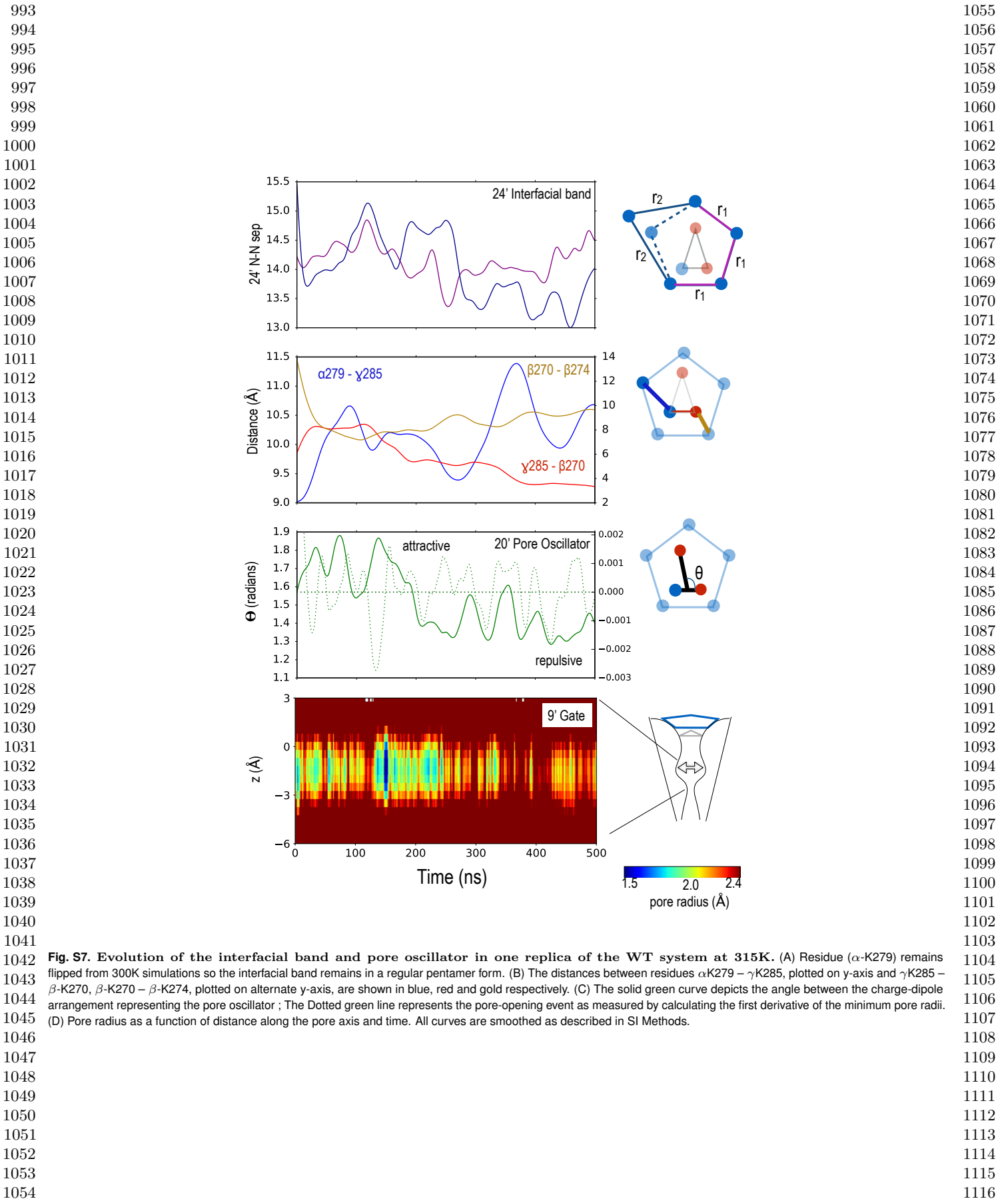


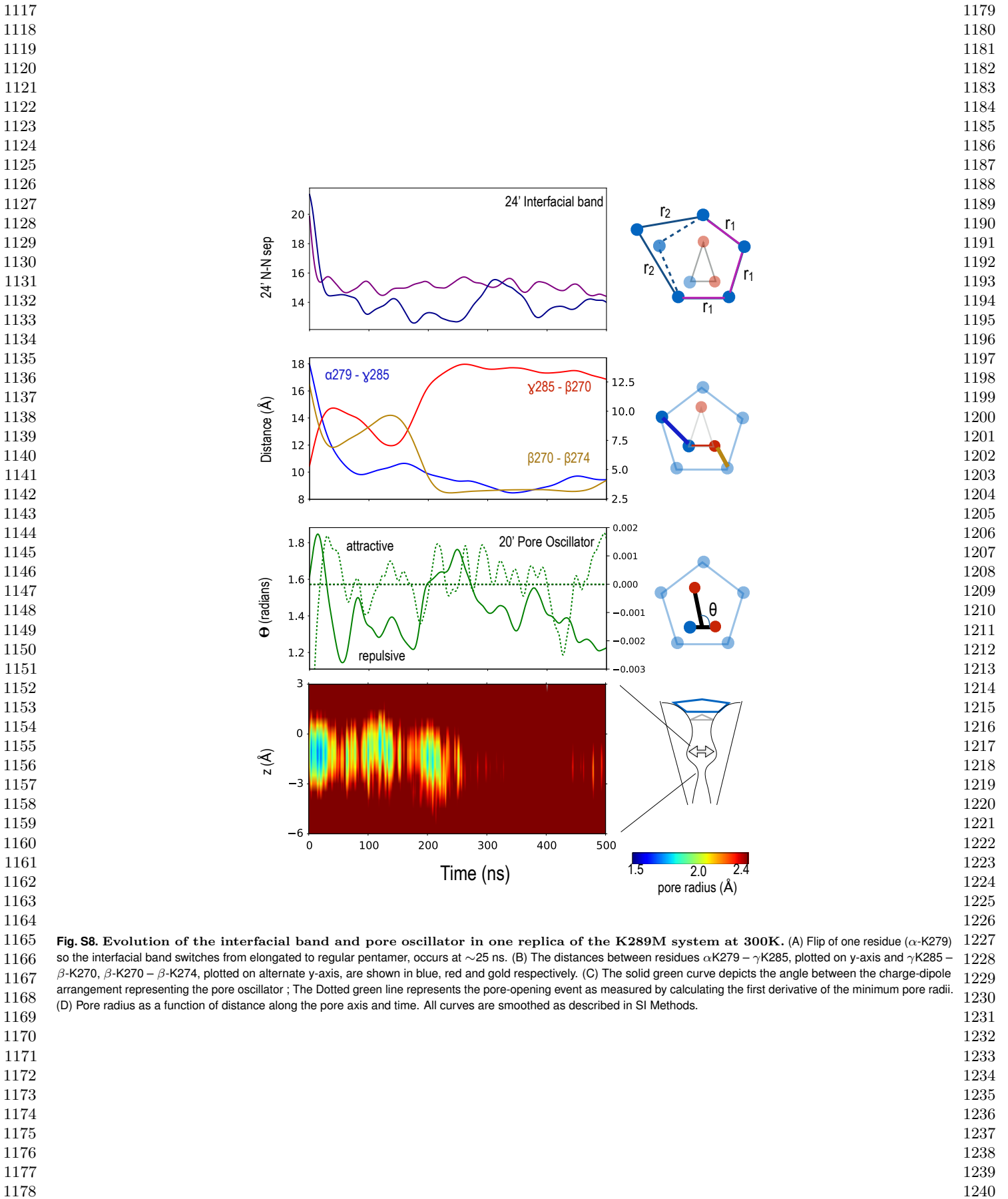
Fig. S4. (A)Number of water molecules along the Z-axis averaged over the frames and replicas. Presence of water in the constriction region of the WT - M2 helices (B) as compared to the temporary dryness due to reduction in pore radii in the K289M - M2 helices(C), at higher temperature.

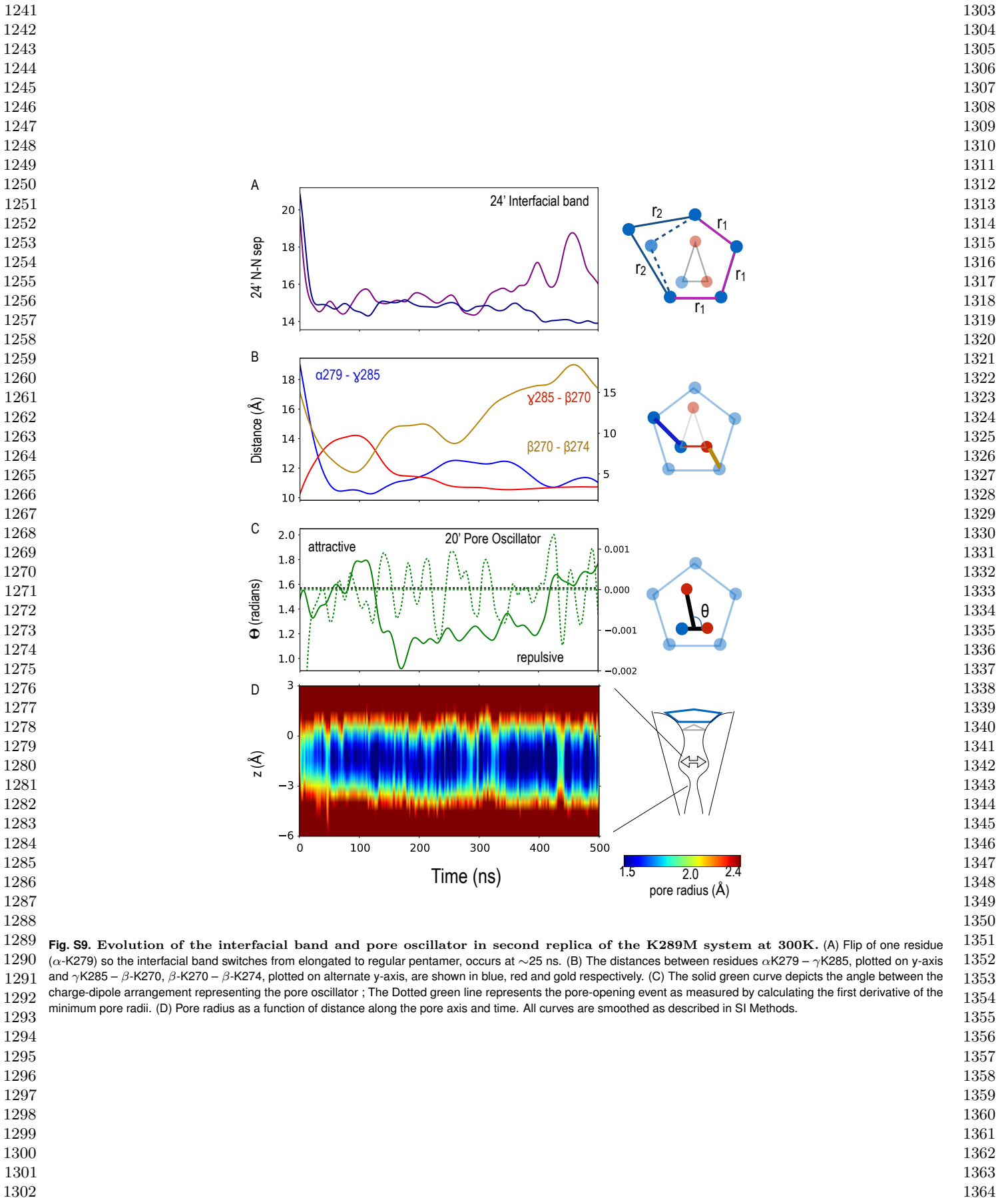
683
684
685
686
687
688
689
690
691
692
693
694
695
696
697
698
699
700
701
702
703
704
705
706
707
708
709
710
711
712
713
714
715
716
717
718
719
720
721
722
723
724
725
726
727
728
729
730
731
732
733
734
735
736
737
738
739
740
741
742
743
744

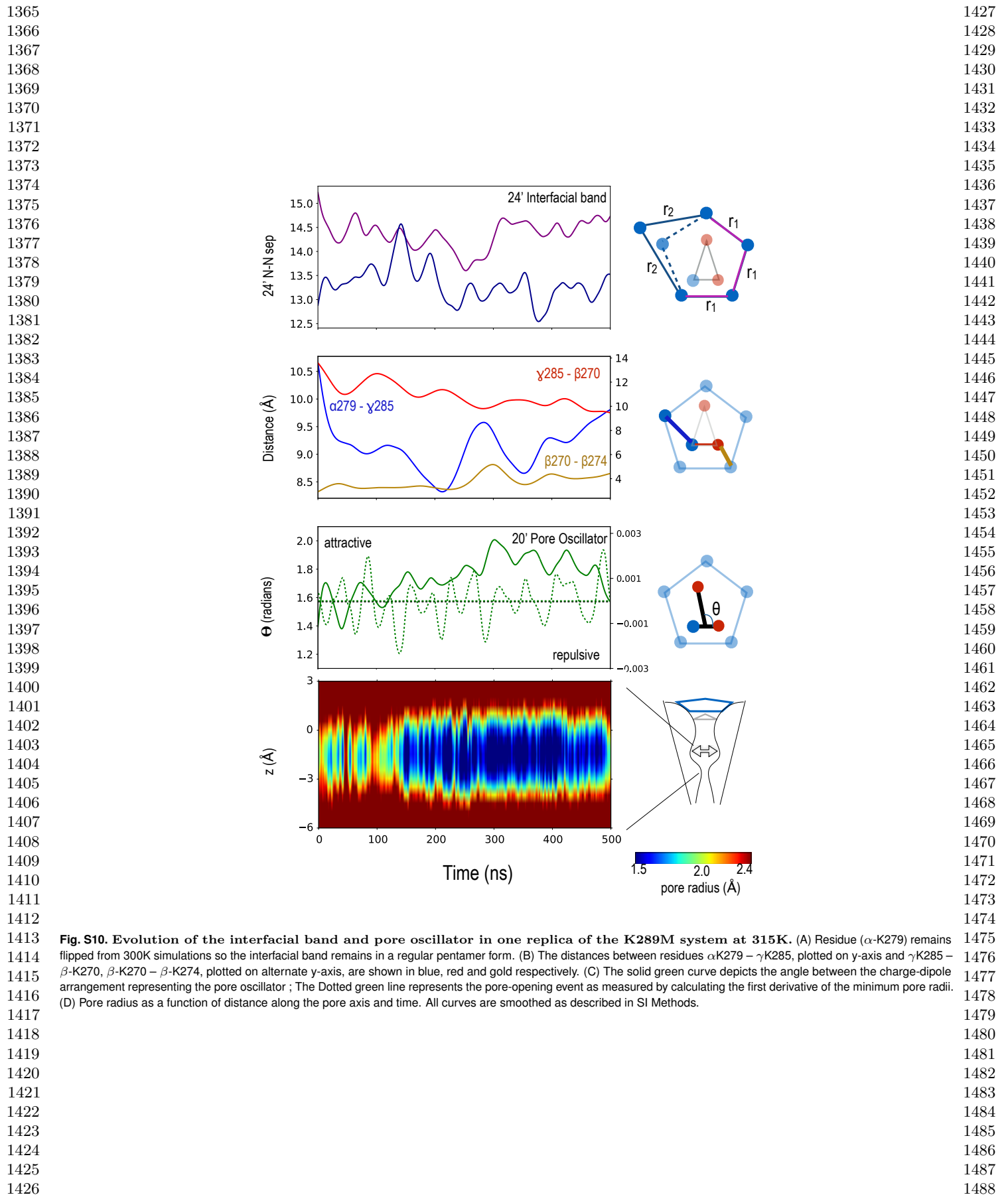


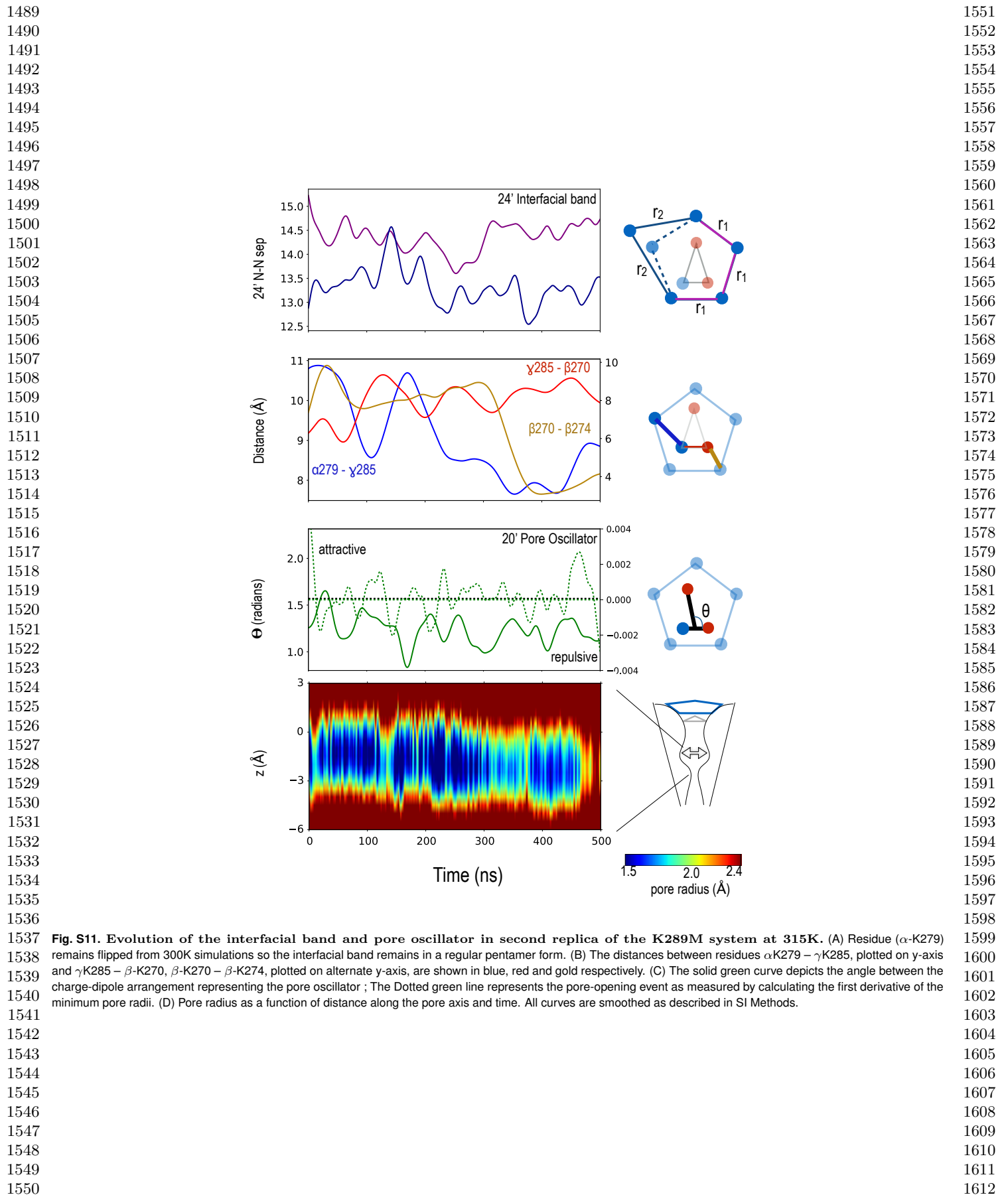












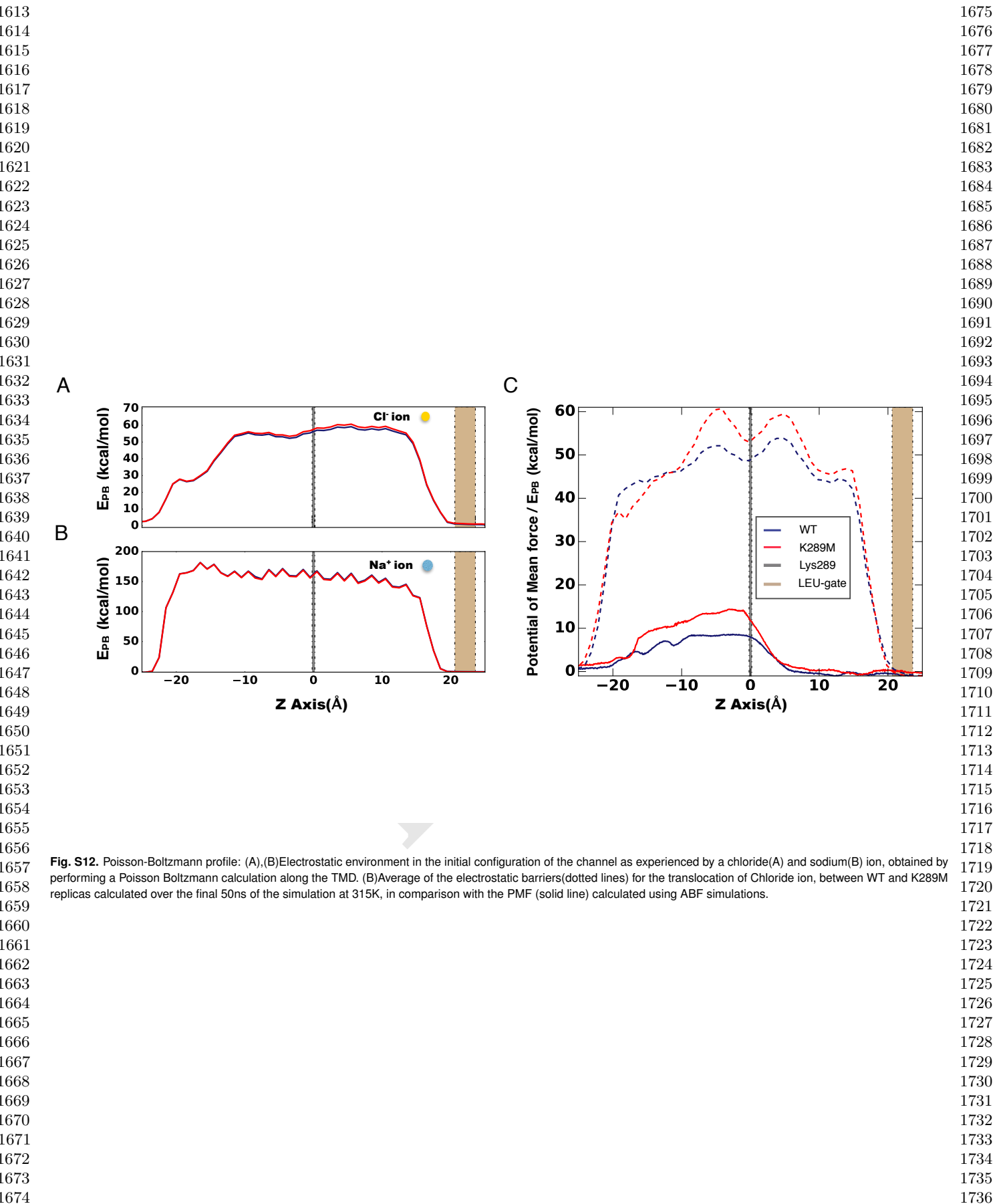


Fig. S12. Poisson-Boltzmann profile: (A),(B)Electrostatic environment in the initial configuration of the channel as experienced by a chloride(A) and sodium(B) ion, obtained by performing a Poisson Boltzmann calculation along the TMD. (B)Average of the electrostatic barriers(dotted lines) for the translocation of Chloride ion, between WT and K289M replicas calculated over the final 50ns of the simulation at 315K, in comparison with the PMF (solid line) calculated using ABF simulations.

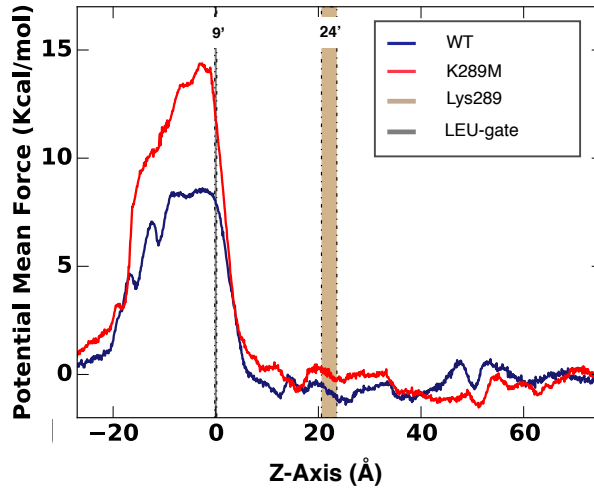
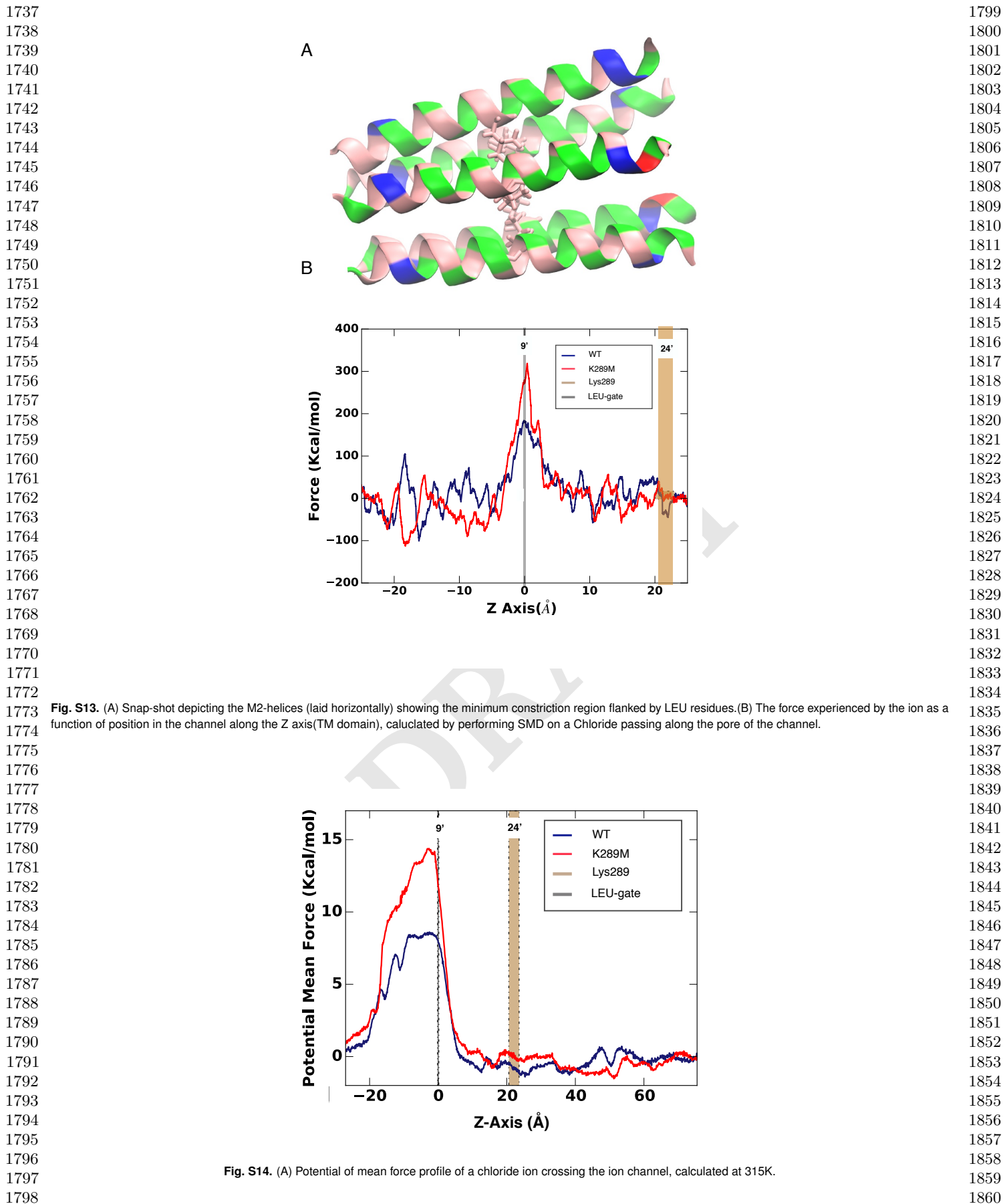


Fig. S14. (A) Potential of mean force profile of a chloride ion crossing the ion channel, calculated at 315K.

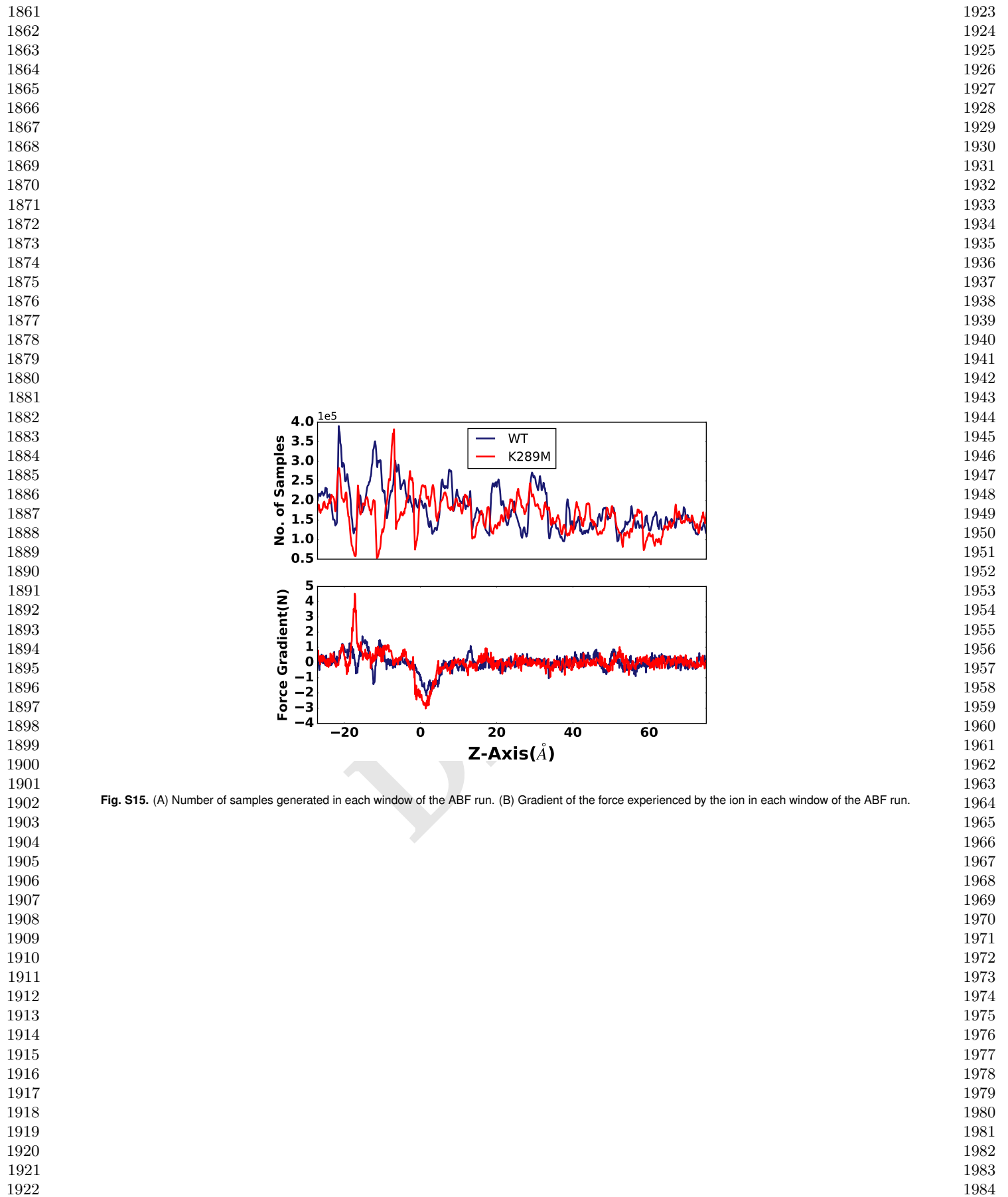


Fig. S15. (A) Number of samples generated in each window of the ABF run. (B) Gradient of the force experienced by the ion in each window of the ABF run.

1985	1. Miller PS, Aricescu AR (2014) Crystal structure of a human GABAA receptor. <i>Nature</i> 512(7514):270–275.	2047
1986	2. Humphrey W, Dalke A, Schulten K (1996) VMD: visual molecular dynamics. <i>Journal of molecular graphics</i> 14(1):33–8, 27–8.	2048
1987	3. Isralewitz B, Baudry J, Gullingsrud J, Kosztin D, Schulten K (2001) Steered molecular dynamics investigations of protein function. <i>Journal of Molecular Graphics and Modelling</i> 19(00):13–25.	2049
1988	4. Park S, Schulten K (2004) Calculating potentials of mean force from steered molecular dynamics simulations. <i>Journal of Chemical Physics</i> 120(2004):5946–5961.	2050
1989	5. Jarzynski C (1997) Nonequilibrium Equality for Free Energy Differences. <i>Physical Review Letters</i> 78(14):2690–2693.	2051
1990	6. Jarzynski C (1997) Equilibrium free-energy differences from nonequilibrium measurements: A master-equation approach. <i>Physical Review E</i> 56(5):5018–5035.	2052
1991	7. Smart OS, Neduvelli JG, Wang X, Wallace BA, Sansom MS (1996) HOLE: a program for the analysis of the pore dimensions of ion channel structural models. <i>J Mol Graph</i> 14(6):354–360,376.	2053
1992	8. Callenberg KM, et al. (2010) APBSmem: A graphical interface for electrostatic calculations at the membrane. <i>PLoS ONE</i> 5(9).	2054
1993	9. Dolinsky TJ, et al. (2007) PDB2PQR: expanding and upgrading automated preparation of biomolecular structures for molecular simulations. <i>Nucleic acids research</i> 35(Web Server issue):W522–5.	2055
1994		2056
1995		2057
1996		2058
1997		2059
1998		2060
1999		2061
2000		2062
2001		2063
2002		2064
2003		2065
2004		2066
2005		2067
2006		2068
2007		2069
2008		2070
2009		2071
2010		2072
2011		2073
2012		2074
2013		2075
2014		2076
2015		2077
2016		2078
2017		2079
2018		2080
2019		2081
2020		2082
2021		2083
2022		2084
2023		2085
2024		2086
2025		2087
2026		2088
2027		2089
2028		2090
2029		2091
2030		2092
2031		2093
2032		2094
2033		2095
2034		2096
2035		2097
2036		2098
2037		2099
2038		2100
2039		2101
2040		2102
2041		2103
2042		2104
2043		2105
2044		2106
2045		2107
2046		2108